Meandering and Eddy Detachment According to a Simple (Looking) Path Equation*

L. J. PRATT

Woods Hole Oceanographic Institution, Woods Hole, Massachusetts

(Manuscript received 7 July 1987, in final form 17 May 1988)

ABSTRACT

Nonlinear meandering and "pinching off" processes are investigated by solving the path equation

$$\partial l/\partial t - \tfrac{1}{2}\,\partial\kappa/\partial x = 0.$$

As shown by Pratt and Stern, this dimensionless equation determines the center line latitude l of a slowly-varying, equivalent barotropic, quasi-geostrophic, f-plane jet with cusped velocity profile and center line curvature $\kappa = l_{xx}/(1 + l_x^2)^{3/2}$. A class of exact solutions consisting of steadily propagating meanders is found having wavelength $2\pi/k$ and amplitude a. The meanders form a wave train which can be single-valued (for $ak < 2.61$) or multivalued (for $2.61 < ak < 8.30$) with respect to the x (eastward) coordinate. For $ak = 8.30$ grazing contact occurs between neighboring meanders and a type of vortex street is formed. The amplitude-dependent dispersion relation for the meanders shows that phase propagation is eastward with speed that increases with decreasing wavelength and/or amplitude, trends observed for Gulf Stream meanders near 72°W by Vazquez and Watts.

Numerical solutions are presented for isolated, single-valued initial disturbances having a characteristic wavenumber k_0 and amplitude a_0. When a_0k_0 is less than a critical value between 1.5 and 2.0, the disturbance disperses. For larger values of a_0k_0, the evolution leads to a "pinching off" phenomenon in which meanders begin to detach from the main portion of the jet and form roughly elliptical eddies.

1. Introduction

Pratt and Stern (1986, hereafter referred to as PS) recently presented a theory describing the nonlinear evolution of meanders of a quasi-geostrophic jet. As sketched in Fig. 1a, the jet flows on an f-plane and is confined to an equivalent-barotropic layer with mean thickness H floating above an inactive lower layer of slightly greater density. The central feature of the jet is that changes in potential vorticity are restricted to a discontinuity occurring across a front separating a northern region of uniform potential vorticity q from a southern region of uniform potential vorticity $q - \Delta q$. The role of the front is to mimic the strong potential vorticity gradient that can occur in the core of currents fed by fluid from widely separated latitudes. In the core of the Gulf Stream for example, the local potential vorticity gradient can be as much as 60 times the planetary potential vorticity gradient (Hall 1985). The simplification to piecewise uniform potential vorticity allows solutions of various initial value problems to be computed using the method of "contour dynamics" (Zabusky et al. 1979; Overman and Zabusky 1982) by which explicit dependence on properties away from the front can be eliminated from the governing equations. Furthermore, the evolution of the flow can be understood in terms of two distinct and often opposing physical processes (explicit in the contour dynamical equations): advection and vortex induction. (The reader is referred to PS as well as Stern and Pratt 1985 and Stern 1985 for more details concerning the use of this method.)

To understand the conclusions of PS and to motivate the present topic, it is helpful to consider the dispersion relation governing infinitesimal disturbances to a basic zonal state. Denoting the dimensional wavenumber k^*, the eastward phase speed of such disturbances is given by

$$c^* = u_0^*[1 - (1 + L_d^2k^{*2})^{-1/2}] \qquad (1.1)$$

where $L_d = (g'H)^{1/2}/f$ is the Rossby radius of deformation, $u_0^* = L_dH\Delta q/2$ is the centerline speed of the jet, and Δq is the potential vorticity difference across the front [the derivation of (1.1) is given in PS]. The first term in the brackets is associated with eastward advection by the jet, while the second term quantifies the westward propagation tendency relative to the jet. The latter is due to vortex induction associated with northward and southward excursions of the front and is analogous to the restoring mechanism in an ordinary Rossby wave (Pedlosky 1979, p. 103). For wavelengths

* Contribution No. 6554 from the Woods Hole Oceanographic Institution.

Corresponding author address: Dr. Lawrence J. Pratt, Clark 3, Woods Hole Oceanographic Institution, Woods Hole, MA 02543.

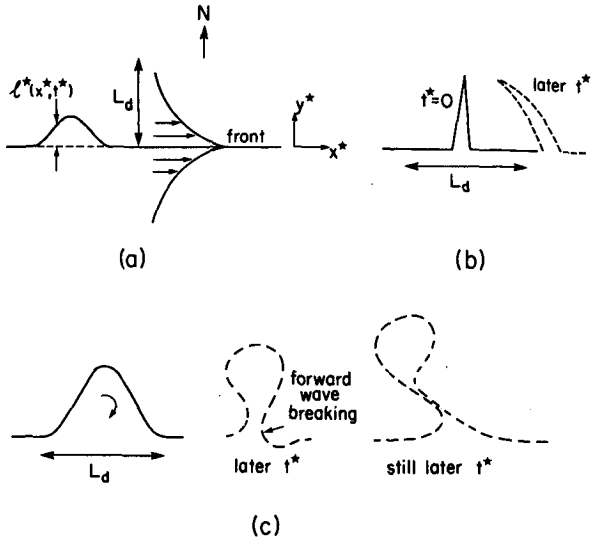

FIG. 1. (a) Definition sketch. In its undisturbed form the jet has a cusped velocity profile centered at the potential vorticity front. (b) Backward wave breaking due to advection by on the cyclonic side of the jet. (c) Forward and backward wave breaking leading to meander detachment.

much shorter than the Rossby radius of deformation ($k^*L_d \to \infty$), $c^* \to u_0^*$ and thus propagation is dominated by advection. Also, PS and Stern (1985) show that the evolution of disturbances having short wavelengths ($k^*L_d \ll 1$) but large [$O(L_d)$] amplitudes is dominated by the advection of the basic flow resulting in the formation of backward breaking waves reminiscent of Gulf Stream shingles, as shown in Fig. 1b.

When the wavelength is of deformation radius scale, $k^*L_d = O(1)$, vortex induction comes into play. Small amplitude disturbances continue to propagate eastward but at a reduced speed. When the disturbance amplitude is as large as L_d, meander lobes can pinch off forming roughly elliptical detached eddies. The detachment is the result of combined forward and backward wave breaking, the latter being associated with the basic shear and the former with a "wrapping around" motion occurring in the opposite sense as the shear. As shown in the third frame of Fig. 1c, forward wave breaking of the isolated ridge becomes most fully developed in an area of relatively weak basic shear while the backward wave breaking develops slightly southward where the basic shear is strongest. As the neck narrows, it becomes stretched into a thin filament, upon which small scale (nonquasi-geostrophic) processes can act. The eddies formed as a result of this detachment bear resemblance to Gulf Stream rings in their shape, isolation, and their ability to transport large volumes of fluid across the jet. For more detailed descriptions of these physical processes, comparisons with observations, and a summary of past numerical work on related problems, the reader is referred to PS.

The object of the present study is to explore the long-wave or "thin jet" limit, in which the radius of curvature of the meanders R is large compared to L_d. It should be noted that the path or surface frontal position of the Gulf Stream, as documented by satellite imagery (e.g., Weatherly et al. 1984), nearly always contains R values extending from $\ll L_d$ to $\gg L_d$. Therefore the model to be presented cannot hope to forecast the detailed behavior of the Gulf Stream or any other midlatitude jet; more sophisticated numerical models designed for that purpose exist (e.g., Robinson et al. 1988). Rather, the object is to set down a result which can serve as a benchmark or reference for establishing physical insight and technical guidance into more structured and realistic models. The attractive feature of the present model is that it is based on a simple physical balance in which a single restoring mechanism (vortex induction) acts, yet the solutions possess a rich behavior bearing qualitative similarity with observed phenomena such as Gulf Stream ring formation. Furthermore, the governing nonlinear equation admits an integral constraint and an exact analytic solution, both of which provide previously unattained predictability and insight into the processes leading to eddy detachment.

Some preliminary insight into the long-wave limit is provided by expanding (1.1) in powers of $k^*L_d \ll 1$, with the result that $c^* \sim (u_0^*/2)(k^*L_d)^2$. Using values $u_0^* = 1$ m s^{-1} and $L_d = 50$ km, which are more or less typical of the Gulf Stream, the phase speed for $k^* = 10^{-2}$ km^{-1} is $c^* = 10.8$ km day^{-1}. This value is surprisingly close to the propagation speed $c_r \approx 11$ km day^{-1} observed by Tracey and Watts (1986) in connection with growing Gulf Stream meanders of small (<10 km) amplitude and the same wavelength (also the longest wavelength reported). The close agreement between the observed and predicted values is, of course, fortuitous; however, the agreement does indicate that (1.1) gives reasonable values. The dispersion relation for long waves also shows that the time scale of motion increases in proportion to the cube of the wavelength. More generally, PS show that finite amplitude configurations of the front having a typical radius of curvature R evolve on a time scale proportional to R^3. By using asymptotic approximations to simplify the contour dynamical equations in the limit $\epsilon = L_d/R \ll 1$, they show that the front evolves according to

$$l_t - \frac{1}{2}\kappa_x = 0 \tag{1.2}$$

where $l(x, t)$ is the latitude of the front,

$$\kappa = l_{xx}/(1 + l_x^2)^{3/2} \tag{1.3}$$

is the frontal curvature, x is longitude, and t is time. All variables have been nondimensionalized using $\epsilon^{-1}L_d$ as a length scale and $\epsilon^{-3}L_d/u_0^*$ as a time scale. Equation (1.2) is valid for $\epsilon \ll 1$ and there is no restric-

tion on wave amplitude or slope. In fact l is allowed to be a multivalued function of x so long as neighboring portions of the front do not come into contact.

The case $\epsilon \ll 1$ can be described as the "thin jet" limit since the distance L_d of lateral velocity decay is small compared to the meander length scale R. This limit has been studied in a variety of contexts, originally by Warren (1963) and most recently by Robinson et al. (1975) and Flierl and Robinson (1984, also see references contained therein). Highly relevant to the case at hand is Robinson et al.'s (1975) study of time-dependent meandering of a thin, quasi-geostrophic jet. Using the vorticity equation as a starting point, they derive an equation for the centerline position of such a jet for general topography and continuous stratification. Although it is possible, in principle, to deduce (1.2) as a special case of their Eq. (3.23) by specializing the coefficients for the present piecewise continuous model, it is much easier to do so by starting with the vorticity equation and reapplying their methods. This derivation is simpler and more intuitive than the derivation of PS and is presented in appendix A.

Although considerable effort has been spent on developing general path equations for thin jets, very little is understood about their nonlinear properties. Most solutions, numerical or otherwise, have been restricted to linearized cases. Equation (1.2) is arguably one of the simplest, fully nonlinear forms that such an equation can take since the physics has been reduced to a "bare bones" level. Despite this, Eq. (1.2) has apparently not been considered previously.

The next section contains several alternative versions of (1.2) which can be used for numerical purposes or which offer additional physical insight. It is shown that one version can be obtained within a constant coefficient using an argument based on the vortex induction effect and symmetry. Also I establish an important integral constraint on l^2 which is used to motivate a finite amplitude instability later observed in the numerical solutions. This instability arises when meanders become multivalued with respect to x and always leads to eddy detachment. Section 3 discusses an exact solution consisting of a periodic meander train propagating with fixed form. If the amplitude a and wavenumber k of the meanders is such that ak = const, the meanders have identical form and differ only in phase speed. For $ak > 2.61$ the form is multivalued with respect to x. This self similarity is used in section 4, where numerical solutions to the initial value problem for an isolated disturbance are discussed. The single valued disturbance has a characteristic amplitude a_0 and wavenumber k_0, and initial values are varied according to their a_0k_0 value. For all cases in which $a_0k_0 > 2.61$ (i.e., the corresponding periodic solution is multivalued), the evolution leads to formation of a detaching eddy. For all but one case in which $a_0k_0 < 2.61$ no detachment occurs. Finally section 5 contains a summary and a statement of implications for future work.

Before proceeding to the analysis, it is worth discussing the philosophy behind the study of large disturbances of linearly stable flows—an approach used in recent studies by Pullin (1981), Stern and Pratt (1985), Stern (1985), Pratt and Stern (1986) and others. To begin with, the introduction of large amplitude disturbances is not in itself unrealistic. East of Cape Hatteras the Gulf Stream is constantly being subjected to large perturbations in the form of variations in the "inlet" condition (i.e., the flow rate and angle near Cape Hatteras). Vazquez and Watts (1985) report events during the angle of the Stream path (here the position of 15°C at 200 m depth) varies continuously by as much as 50° over the dominant 33–50 day meander periods. More pertinent to the "large disturbance" approach is the need to identify and quantify strongly nonlinear processes which dominate once an infinitesimal instability saturates. The expectation is that the strongly nonlinear processes occurring in the simpler, linearly stable models will arise to some extent in linearly unstable models.

2. Alternative forms and physical interpretations of the path equation

It is possible to derive a number of alternative forms of (1.2) which aid the physical intuition and can be useful numerically. Let s denote arclength along the front, measured so that s increases with high potential vorticity to the left, and let Θ denote the angle between the tangent to the front and the x-axis, as shown in Fig. 2. The curvature κ of the front is given by $\partial\Theta/\partial s$ and the differential arclength ∂s along the front is given by $\partial x/\cos\Theta$. Finally, denoting the differential displacement $\partial l \cos\Theta$ of the front normal to itself (and to the left of positive ∂s) by $\partial l'$, Eq. (1.2) can be rewritten

$$\partial l'/\partial t - \tfrac{1}{2}\,\partial\kappa/\partial s = 0 \qquad (2.1)$$

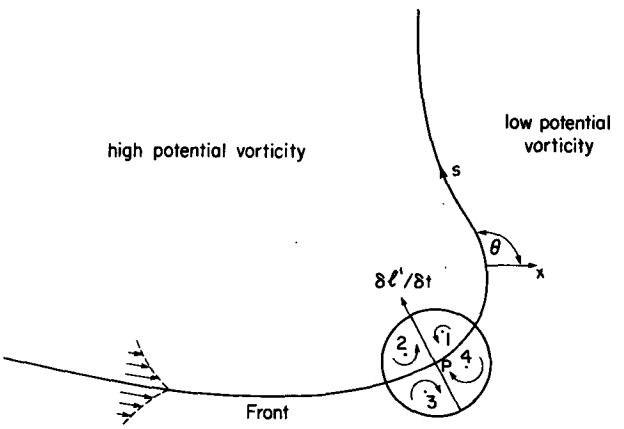

FIG. 2. The vortex induction effect acting within a circle of radius L_d about a point at which the curvature increases with arclength s.

or alternatively

$$\partial l'/\partial t - \tfrac{1}{2}\,\partial^2\Theta/\partial s^2 = 0. \qquad (2.2)$$

Despite their simple form, these equations are not particularly well suited to analysis analytically due to the complexity of the relationship between l' and κ and between l' and Θ. However Eq. (2.1) does form the basis for the algorithm used to calculate the numerical solutions presented later, and the reader is referred to appendix B for details.

In physical terms Eqs. (2.1) and (2.2) can be motivated using an argument based on the vortex induction effect. It will be convenient to temporarily relax the restriction to small curvature, so that the variables s, κ, etc. need no longer reflect slow variations with respect to L_d (i.e., the scaling factor $\epsilon \ll 1$ is temporarily absent). Consider a point P on the front as shown in Fig. 2. The rate of displacement $\partial l'/\partial t$ of the front normal to itself at P is equal to the normal velocity, and the latter is induced by the point vortices lying within a deformation radius or so of P. If a circle of radius L_d is drawn about P, the quadrants labeled 2 and 4, whose vorticity tends to move the front northwest, have greater total area than quadrants 1 and 3, whose vorticity tends to move the front southeast. The area mismatch implies that the front will move in the northwest direction (i.e., $\partial l'/\partial t > 0$). This tendency can be quantified by noting that $\partial l'/\partial t$ depends at most upon the configuration of the front relative to P, a fact which can be established using the method of contour dynamics [see PS, Eq. (3.3)]. That is, $\partial l'/\partial t$ depends at most upon the derivatives of Θ with respect to s at P, since these determine the coefficients in the Taylor series expansion of $\Theta(s)$ about P. Furthermore, no dependence upon Θ itself should exist, since Θ is defined with respect to an arbitrary reference, hence

$$\partial l'/\partial t = F(\Theta_s, \Theta_{ss}, \Theta_{sss}, \text{etc.}). \qquad (2.3)$$

No restriction to small curvature has been made; however, if we now let $\Theta = \Theta(\epsilon s)(\epsilon \ll 1)$, substitute into F and replace ϵs by s, the result can be written

$$F(\epsilon\Theta_s, \epsilon^2\Theta_{ss}, \cdots) = \epsilon F_1\Theta_s + \epsilon^2 F_2\Theta_{ss} + O(\epsilon^3).$$

The constants F_1, F_2, etc. determine the coefficients in the asymptotic expansion of F in powers of ϵ. Returning to Fig. 2, it is clear that F_1 must vanish since any circular arc (Θ_s = const) intersecting the circle results in equal areas between quadrants (2 plus 4) and (1 plus 3) and thus no restoring tendency. Within an $O(\epsilon)$ error the rate of lateral displacement of the front is proportional to Θ_{ss} and Eq. (2.2) is recovered in form. In Fig. 2, it can be seen that greater area of quadrants 1 and 3 is due to the increasing curvature ($\Theta_{ss} > 0$) of the gradually varying front.

Alternative physical interpretations can be made by considering the mass and vorticity budgets for a fixed box through which the jet passes. These budgets are discussed in detail in the alternate derivation of (2.1) (appendix A). In terms of mass conservation, it is shown that $\partial l'/\partial t$ measures the change in fluid volume in the box associated with lateral motions of the front. These motions cause relatively deep, low potential vorticity fluid or relatively shallow, high potential vorticity to move in and out of the box. The term $\frac{1}{2}\,\partial\kappa/\partial s$ measures the divergence in the ageostrophic velocity field which must balance the volume change. In terms of the vorticity budget, the volume change associated with $\partial l'/\partial t$ implies a net vortex stretching or squeezing which must be balanced by a net export or import of vorticity. The latter is measured by advection of the curvature term in the expression for vorticity in an intrinsic coordinate system and leads to the term $\frac{1}{2}\,\partial\kappa/\partial s$.

It is possible to derive a single equation for l by substituting the cartesian expression for curvature (1.3) into (1.2), giving

$$l_t - \tfrac{1}{2}\,l_{xxx}\Big/[(1 + l_x^2)^{3/2}] + \tfrac{3}{2}\,(l_{xx}^2 l_x)\Big/[(1 + l_x^2)^{5/2}] = 0. \qquad (2.4)$$

[Although this equation has some cosmetic similarity to the KdV equation and other well-known nonlinear dispersive equations (Whitham 1974), the solutions to (2.3) are quite unlike those of the others, as will be shown presently.]

For disturbances which are isolated in x (so that H vanishes as $x \to \pm\infty$) there are several important integral constraints which should be pointed out. Integration of (2.1) over the entire arclength of the curve yields

$$\int_{-\infty}^{\infty} (\partial l'/\partial t)\,ds = \int_{-\infty}^{\infty} \cos\Theta(\partial l/\partial t)\,ds = 0.$$

Using $dx = \cos\Theta ds$, this result can be written

$$\partial/\partial t \int_{-\infty}^{\infty} l\,dx = 0 \qquad (2.5)$$

where the x-integration is understood to cover all values of s in multivalued cases. Equation (2.5) states that the total area under an isolated disturbance remains constant and increases in the area of wave crests must be compensated for by increases in trough area. The same result applies if l is periodic with respect to x and the integration is made over one wavelength.

A similar result can be obtained with respect to energy by multiplying (1.2) by l and performing several integrations by parts. The result

$$\frac{\partial}{\partial t}\left(\frac{l^2}{2}\right) - \frac{\partial}{\partial x}\left[\frac{\kappa l + (1 + l_x^2)^{-1/2}}{2}\right] = 0 \qquad (2.6)$$

has the form of a finite amplitude conservation law for

wave action (Andrews and McIntyre 1978). Integration over the entire arclength of the curve in the manner just described yields

$$\partial/\partial t \int_{-\infty}^{\infty} l^2 dx = 0 \qquad (2.7)$$

for isolated disturbances. For single-valued l, (2.7) severely restricts any disturbance growth that might occur as the result of a finite-amplitude instability; increases in $|l|$ in one region must be compensated for by decreases elsewhere. For multivalued disturbances, however, $|l|$ can grow without compensation due to the fact that negative values of dx arise in (2.7).

The steady solution to (1.2) is obtained most easily from the alternate form (2.2). Setting $\partial/\partial t = 0$ leads to Θ as $\alpha s + \beta$, which describes a circle of radius α^{-1}. When $\alpha = 0$ the solution reduces to a straight line of angle β measured counterclockwise from the x-axis.

Finally, for the benefit of future investigators, I note that (1.2) admits the similarity solution $l = (t - t_0)^{1/3} F(\xi)$, where $\xi = x/(t - t_0)^{1/3}$ and

$$(F - \xi F') - \frac{3}{2}[F''(1 + F'^2)^{3/2}]' = 0.$$

However, numerical integrations of this equation failed to produce any physically meaningful solutions.

3. Large amplitude meanders of permanent form

It is possible to find an exact solution to (2.4) by looking for values of l (or Θ), which are stationary in a moving frame of reference. Writing $l = l(x - ct)$ and substituting this functional form into (2.4) leads to

$$d(\kappa + 2cl)/d(x - ct) = 0. \qquad (3.1)$$

The intrinsic coordinates Θ and s are now used, with s representing an arclength coordinate fixed in a frame of reference moving eastward at speed c, so that

$$x - ct = x_0 - ct_0 + \int_0^{\tilde{s}} \cos\Theta(\hat{s}) d\hat{s} \qquad (3.2)$$

$$l(\tilde{s}) = l_0 + \int_0^{\tilde{s}} \sin\Theta(\hat{s}) d\hat{s}. \qquad (3.3)$$

Thus κ may be replaced by $d\Theta/d\tilde{s}$, $d/d(x - ct)$ by $(\cos\Theta)^{-1} d/d\tilde{s}$ and (3.1) is transformed into the pendulum equation:

$$d^2\Theta/d\tilde{s}^2 + 2c \sin\Theta = 0. \qquad (3.4)$$

Equation (3.4) arises in the theory for the buckling of columns (Timoshenko and Gere 1961) and was also used as a model equation by Masuda (1982) to study the path of the Kuroshio. Periodic solutions may be written in terms of elliptic functions and the reader will find an expose in either of these references. The solutions form a curve known as an elastica, and two examples are shown in the upper right of Fig. 3. Note

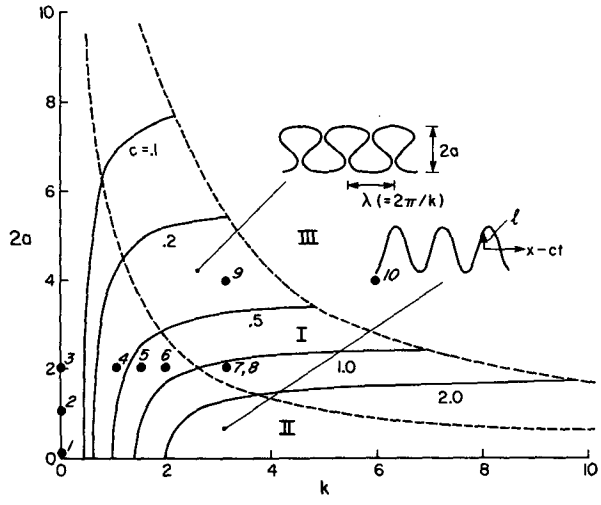

FIG. 3. Nonlinear dispersion diagram for steadily propagating meanders. The solid curves are curves of constant phase speed. Above the lower dashed line ($ka = 2.61$) the meanders are multivalued. Above the upper dashed line ($ka = 8.30$) the meanders intersect each other and are disallowed. The curve $c = 1$ also gives values of $Hc^{1/2}$ when the ordinate is replaced by $k/c^{1/2}$. The numbered dots indicate values of $k = k_0$ and $a = a_0$ used in initial value problems for isolated disturbances.

that the meanders may be multivalued with respect to $x - ct$, as in the case of the upper curve. When the folding of the curve becomes so severe that neighboring meanders touch, the geometric assumptions upon which the theory is based are violated. For meanders of small slope the elastica reduces to the sinusoidal meanders discussed in the last section.

Although the dispersion relation for the meandering solutions may be plotted using the elliptic function solutions, it is just as easy to do so by solving (3.4) numerically. Here an Adams method (Gear 1971) was used to integrate (3.4) and the solution was transformed back to $(x - ct, l)$ coordinates using numerical approximations to (3.2) and (3.3). By varying $\Theta(0)$ and $\Theta'(0)$ a variety of periodic solutions is produced having amplitude a and wavelength λ, as defined in Fig. 3. Figure 3 shows the curves of constant wave speed c as a function of amplitude and wavenumber $k = 2\pi/\lambda$. In the region bounded by the horizontal and vertical axes and the lower dashed line (region I) the meanders are single valued. Between the two dashed lines (region II) the meanders are multivalued. Above the upper dashed line (region III) the meanders intersect. Note that the wave speed is positive (the meanders move eastward) for all wavelengths, as hinted at by the weakly nonlinear expression for phase speed (3.6). Increasing amplitude and/or wavelength tend to decrease the wave speed, trends observed by Vazquez and Watts (1985) to be features of growing Gulf Stream meanders near 72°W (slightly east of Hatteras). Finally, note that the multivalued meanders tend to be weakly dis-

persive with respect to k ($\partial c/\partial k$ is small) and strongly dispersive with respect to a. The opposite is true of the single valued meanders.

It is natural to ask whether (2.4) admits a solitary wave solution (i.e., a wave of permanent form and infinite wavelength). Inspection of Fig. 3 reveals that $c \to 0$ as $k \to 0$ for any fixed amplitude. Thus, any solitary wave solution would necessarily be a steady ($c = 0$) solution. It has already been shown that the only possible steady solutions are the line and the circle. The circle is similar to a solitary wave solution in that it is a finite-amplitude, isolated disturbance with permanent form. However, no propagating, solitary wave of permanent form exists.

Although Fig. 3 displays propagation information in a convenient and readily available manner, the information contained therein is redundant in the sense that the solutions possess a degree of self-similarity. In fact it can be shown that along any curve ka = const the meanders are differently magnified versions of a fixed shape. To do so, introduce the stretched variable $\hat{s} = \tilde{s}c^{1/2}$ into (3.4), thereby eliminating the coefficient c from the equation. The procedure for calculating the solutions can then be repeated yielding a curve of $k/c^{1/2}$ versus $c^{1/2}a$ values. This curve is identical to the $c = 1$ curve in Fig. 3 when the ordinate and abscissa are replaced by $k/c^{1/2}$ and $2c^{1/2}a$, respectively. Direct numerical calculation of this curve shows that the boundary separating single valued from multivalued meanders lies at $k/c^{1/2} \approx 2.61$ and $c^{1/2}a \approx 1.00$, or $ka \approx 2.61$. The boundary separating multivalued from intersecting solutions lies at $ka \approx 8.30$.

The similarity property has the following meaning for the periodic solutions. Suppose one chooses such a solution having wavenumber, amplitude and speed k_0, a_0 and c_0. Then any other solution having k and a such that $ka = k_0a_0$ possesses identical form, and its propagation speed is inversely proportional to the square of the magnifying factor. Thus the self similar meander having amplitude $2a_0$ has speed $c_0/4$. One importance of this finding is that it restricts the range of initial conditions which must be explored in the numerical experiments (section 4).

The limiting case of ka slightly less than 8.30 describes a type of vortex-street solution for which the meander lobes (which nearly experience grazing contact with each other) form two rows of staggered eddies. The aspect ratio a'/b' of this solution (a' and b' are the y- and x-separation between vortex centers of opposite sign) is $ak/2\pi = 1.32$. Now Flierl et al. (1987) have found stable vortex-streets with a'/b' ranging from 0.24 to 0.50 in numerical calculations of finite amplitude motions resulting from barotropic jet instability with $\beta = 0$. There are many differences between the model used by Flierl et al. and the one considered here (in their calculation the deformation radius is essentially infinite and the vortex-streets do not have a long-wave character), however, the suggestion is that the meander solutions with ka values near 8.30 are unstable. Note also that the lowest value of $ak/2\pi$ that a multivalued meander can have (corresponding to the $ka = 2.61$ solution) is 0.42, which corresponds to a stable vortex street. Together with the integral constraint (2.7), this result leads to the conjecture that some or all of the multivalued solutions may be unstable, a hypothesis supported by numerical simulations presented next.

4. Time-dependent numerical solutions for isolated disturbances

I now discuss the results of a set of initial value problems in which solutions to (1.2) are obtained numerically. The general philosophy in these problems is to choose an isolated initial disturbance having a dominant wavenumber and amplitude, allowing Fig. 3 to be used as an aid in interpreting results. To this end, the single-valued initial condition

$$l(x, 0) = a_0 e^{-(x/w)^2} \cos(k_0 x) \tag{4.1}$$

is chosen. The Fourier transform of $l(x, 0)$ is

$$(wa_0/2^{1/2}) e^{-w^2(k-k_0)^2/4}$$

indicating that k_0 is the dominant wavenumber. The length scale w determines the extent to which wavelengths neighboring k_0 are present. The procedure is to vary a_0 and k_0 between initial value experiments, while w is kept constant for the most part. Table 1 lists the parameter settings for each numerical run and the values of k_0 and a_0 for each run are also indicated in the nonlinear dispersion diagram for periodic meanders (Fig. 3). In accordance with the similarity property mentioned in the last section, a_0 and k_0 variations *along* curves a_0k_0 = const were avoided in favor of variations *normal* to a_0k_0 = const curves. This selection was made with the anticipation that the former would lead to solutions whose qualitative behavior would differ mainly in time scale.

None of the standard numerical procedures for integrating the Korteweg–de Vries equation or related evolution equations are well suited to the present problem. The term $(1 + l_x^2)^{1/2}$ makes the spectral approach (Fornberg and Whitham 1978) awkward, and both forward and centered time stepping in connection with spatial finite differencing (Vliegenthart 1971) were found to be numerically unstable. A scheme which avoids these problems is the leapfrog trapezoidal method (Haltiner and Williams 1980). As described in appendix B, this method contains elements of both forward and centered time differencing and has been modified to be compatible with an intrinsic coordinate system. The method is conditionally stable, although the time step required for stability of calculations involving highly curved initial conditions can be exceedingly small. In fact, some of the calculations required 1 cpu hour or more on a Cray X-MP supercomputer.

TABLE 1. List of parameters for numerical experiments. The initial condition is given by Eq. (5.1).

Run	a_0	k_0	w	Description of initial condition	Results
1	0.05	0	1	isolated disturbance with small amplitude and wave number = 0	disturbance completely disperses
2	0.5	0	1	same as Run 1 but larger amplitude	disturbance completely disperses
3	1.0	0	1	same as Run 2 but larger amplitude	disturbance completely disperses
4	1.0	1.0	1	same as Run 3 but finite wavenumber	disturbance completely disperses
5	1.0	1.5	1	same as Run 4 but larger wavenumber	disturbance completely disperses
6	1.0	2.0	1	same as Run 5 but larger wavenumber	eddy pinches off at $t = 16.66$
7	1.0	3.0	1	a_0 and k_0 now in region of multiply valued meanders of Fig. 3	eddy pinches off at $t = 13.96$
8	1.0	3.0	2	same as Run 5 but more oscillations	eddy pinches off at $t \approx 6.45$
9	2.0	3.0	1	same as Run 5 but larger amplitude	eddy pinches off at $t \approx 4.18$
10	2.0	6.0	1	same as Run 7 but larger wavenumber	eddy pinches off at $t \approx 0.072$

Table 2 gives the maximum stable time step found for various degrees of resolution.

As a test of the numerical code, a comparison was made between the computed solution for the small amplitude case $a_0 = 0.05$, $w = 1$, $k_0 = 0$ and the exact solution of the linearized version of (1.2):

$$\partial l/\partial t - \frac{1}{2}\partial^3 l/\partial x^3 = 0 \qquad (4.2)$$

for the same initial condition. This solution can be obtained by elementary methods and is given by

$$l(x, \tau) = 0.5(\pi)^{-1/2} \int_0^\infty e^{-(kw/2)^2} \times \cos\left(kx - \frac{1}{2}k^3 t\right) dk. \qquad (4.3)$$

Figure 4 shows the numerical solution at times $t = 0$, 1.2 and 2.0 computed using spatial resolution $\Delta s = 0.1$ and time step Δt at 0.0008. Some sample values of the exact linear solution at $t = 2$ have been indicated using crosses. Using the previously mentioned $k^* = 10^{-2}$ km^{-1}, $c^* = 10.8$ km day^{-1} wave as a basis for scaling, the dimensionless time $t = 1$ corresponds to 62.5 days or about 2 months. The difference in l between the linear and numerical solutions at $t = 2$ is typically 0.0001 and this difference may largely be due to weak nonlinear effects. In addition two numerical runs at different resolutions were carried out over a portion of the worst (i.e., highest required resolution and least stable) case—the $t = 0$ to $t = 0.007$ segment of Run 8 (see Fig. 6). This test compared results with average resolutions of $\Delta s = 0.023$ and $\Delta s = 0.015$ and

TABLE 2. Maximum stable time steps found (by trial and error) for various degrees of resolution in numerical method.

Δs	Δt
0.008	$(1.0 \pm 0.3) \times 10^{-7}$
0.014	$(5.0 \pm 1) \times 10^{-7}$
0.023	$(2.8 \pm 0.2) \times 10^{-6}$
0.040	$(4.0 \pm 0.04) \times 10^{-5}$
0.052	8.0×10^{-5}
0.072	2.0×10^{-4}
0.080	2.3×10^{-4}
0.100	$(6.0 \pm 1) \times 10^{-4}$

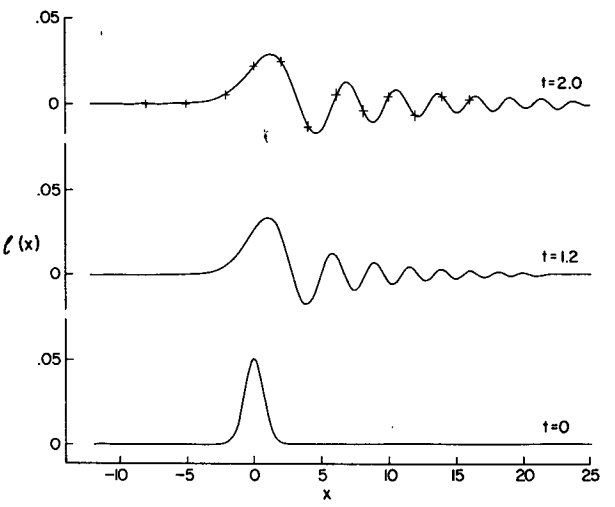

FIG. 4. Numerical solution to "linear" initial condition $a_0 = 0.05$, $k_0 = 0$, $w = 1$. (Run 1). The crosses indicate the exact linear solution at $t = 2$. For Gulf Stream scaling $t = 1$ corresponds to roughly 2 months.

found positional discrepancies of less than 0.3% of a_0. (Although the time interval 0.007 appears short, the front evolves rapidly due to the large initial values of $\partial\kappa/\partial s$. The time step needed for computational stability in the high resolution case is as low as 10^{-8}, requiring over 1 Cray cpu hour to run).

Runs 2, 3, 4 and 5 have a_0 and k_0 settings lying within region I of Fig. 3 and all exhibit the same dispersive behavior as the linear case (Run 1). Figure 5 shows the evolution of the front for Run 3, in which k_0 is the same as run 1 but a_0 has been increased to unity. (In Fig. 5 the horizontal axis has been compressed making the disturbances appear much more "spiked" than is actually the case.) As shown, the initial lump disperses in the east (downstream) direction with the smaller amplitudes and wavelengths outrunning the larger amplitudes and wavelengths. At $t = 9.7$ the maximum values of $|l|$ and $|\partial l/\partial x|$ have decayed by factors of 2 to 3 over their initial values indicating that no wave breaking will occur in the foreseeable future.

Runs 7, 8 and 9 have (a_0, k_0) values lying in region II of Fig. 3 ($2.61 < k_0 a_0 < 8.3$). That is, if the initial condition was a member of the group of previously-described elastica with amplitude a_0 and wavenumber k_0, then the elastica would be multiply valued with respect to x. Of course, the actual initial condition (5.1) is always single-valued. Run 10 has (a_0, k_0) values lying in region III of Fig. 3 ($ka > 8.3$), i.e. the corresponding elastica would intersect itself. All four of these runs exhibit behavior dramatically different from Runs 1–4. Perhaps the easiest to understand is Run 10, which will be discussed first.

Figure 6 shows the results for Run 10 ($a_0 = 2$, $k_0 = 6$). At $t = 0.001$ in Fig. 6, trains of short waves have appeared in the lees of the meander tips of the initial profile. Despite appearances, these waves are not numerical instabilities; each wavelength is well resolved in the numerics with the profile at $t = 0.001$, for example, having roughly 18 points per small wavelength in the original run and roughly 30 points per wavelength in the repeat run. The short waves will be referred to as "secondary" while the larger meanders present in the initial data will be called "primary." The secondary waves move much more rapidly than the primary waves and therefore propagate on the initial profile as if it was a steady basic state. At $t = 0.007$ and $t = 0.043$ we see slower, longer secondary waves in the lees of the meander tips. The amplitudes of the secondary waves are larger than earlier, giving the front a more contorted shape overall. The arrows drawn on the $t = 0.043$ profile indicate two secondary wave crests, one moving southward and the other northward. At $t = 0.072$ the tips of the crests have collided, causing the front to intersect itself.

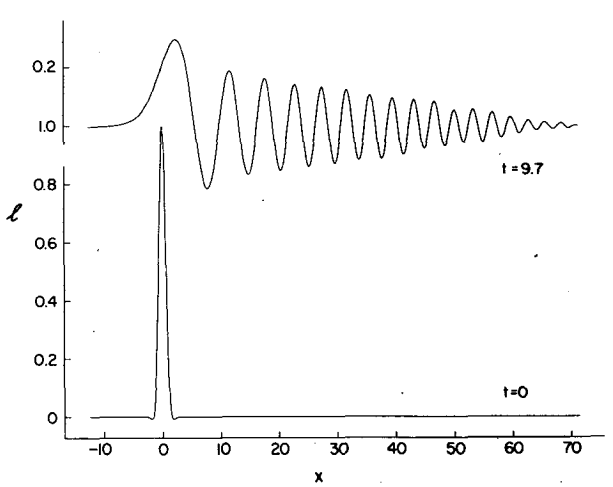

FIG. 5. Numerical solution, Run 3; $a_0 = 1$, $k_0 = 0$, $w = 1$.

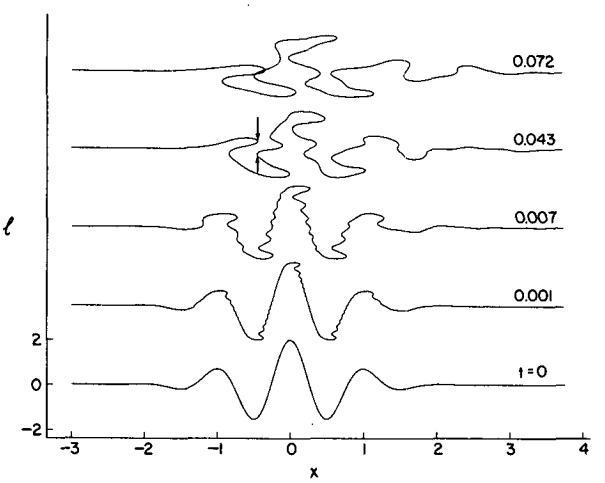

FIG. 6. Numerical solution, Run 10; $a_0 = 2$, $k_0 = 6$, $w = 1$. For Gulf Stream scaling $t = 0.072$ corresponds roughly to 5 days.

When grazing contact occurs between separate segments of the front, the assumptions forming the basis of Eq. (1.2) are violated and the integration should be stopped. In Fig. 6 the numerical integration has been stepped slightly past the point of grazing contact. The time scale for pinching off can be estimated by computing the level time t_P required by a secondary wave to propagate over half the arclength Δs of the primary meander lobe. For the lower left lobe of the $t = 0$ profile in Fig. 6, $\Delta s \approx 1$. Using a secondary wavelength $\Delta s/2$, for which the linear group speed is $C \approx 14.8$, one obtains

$$t_P \approx \Delta s/(2C) \approx 0.034$$

as compared with the observed $t_P = 0.072$ (or about 5 days). This estimate can be refined using Fig. 3 to account for amplitude effects.

Runs 7, 8 and 9 (which have initial conditions lying in region II of Fig. 3) also exhibit eddy detachment, but the time scale required is much longer and the physics more subtle. Runs 7 and 8 are made using the same values $a_0 = 1$ and $k_0 = 3$, but different values of

w ($w = 1$ for Run 7 and $w = 2$ for Run 8). Note that (a_0, k_0) lies near the boundary between regions I and II in Fig. 3. Both runs behave similarly and I discuss only Run 8 in detail (see Fig. 7). Although short secondary waves appear shortly after $t = 0$ (not visible in Fig. 7), these waves do not lead to immediate eddy detachment. By time $t = 0.04$ the wavelengths of the secondary waves are as large as those of the primary waves and it becomes futile to distinguish between the two. As time increases, some of the energy in the initial disturbance escapes to the east in the form of packets of relatively small amplitude waves. One such packet is particularly visible between $x = 20$ and $x = 30$ at $t = 3.72$. At the same time a coherent region of larger amplitude motion remains near $x = 0$, drifting slowly eastward. This positioning is consistent with the nonlinear dispersion relation which indicates the retarding effect of wave amplitude on speed. Multivalued shapes appear in the large amplitude region after about $t = 0.35$ and are particularly noticeable in the $t = 0.59$, $t = 1.2$ and $t = 2.71$ profiles. As more energy is lost to the east, the large amplitude region reduces to a single lobe which grows in amplitude and fluctuates in north–south polarity (compare the $t = 0.86$, 1.79, 3.72, and 6.45 profiles). At $t = 6.45$ this lobe begins to pinch off and the integration is halted.

One of the remarkable features of Run 8 is the amplitude growth experienced by the main lobe. Figure 8 gives the maximum value of $|l|$ as a function of t and shows a nearly three fold increase in amplitude by the time grazing contact occurs. Thus the flow experiences a finite amplitude instability, which is evidently instrumental in inducing meander detachment. No sign of such an instability was seen in the region I numerical runs nor in the analysis of weakly nonlinear effects (section 3). The tendency for growth of multivalued, rather than single-valued, disturbances is suggested by the integral constraint (2.7), as discussed earlier.

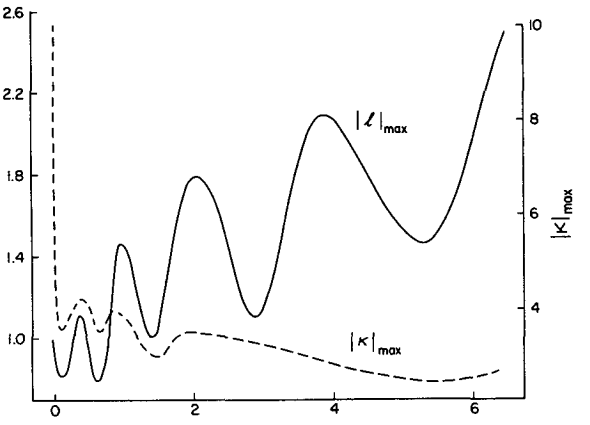

FIG. 8. Max$|L|$ and max$|\kappa|$ vs time for Run 8.

Also plotted in Fig. 8 is the maximum value of $|\kappa|$ versus time. Shortly after $t = 0$, $|\kappa|$ decreases from a value of 10 to about 4. This rapid decrease is due to the secondary waves, which disperse concentrations of high curvature. After the sudden initial decrease, $|\kappa|_{max}$ experiences more gradual decreases as the curvature is dispersed by longer wave lengths and larger amplitudes. The occurrence of wave breaking and the formation of closed eddies is consistent with the dispersion of curvature in the sense that curves with evenly distributed curvature with respect to s tend to be multivalued with respect to x. The simplest example is the circle, which contains uniformly distributed curvature with respect to s. As noted earlier, the circle is the only exact steady solution to (1.2) (aside from the straight line).

Figure 9 shows the results for Run 9 ($a_0 = 2$, $k_0 = 3$, $w = 1$). Here (a_0, k_0) lies near the boundary between regions II and III in Fig. 3. The evolution for this case is similar to that of Run 8 except that two isolated regions having relatively large amplitudes de-

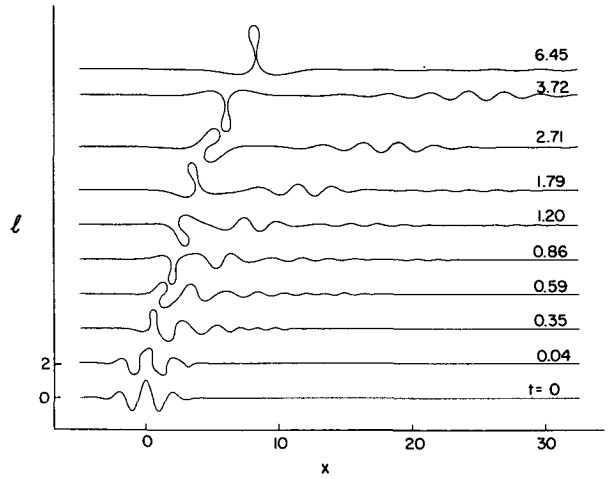

FIG. 7. Numerical solution, Run 8; $a_0 = 1$, $k_0 = 3$, $w = 2$.

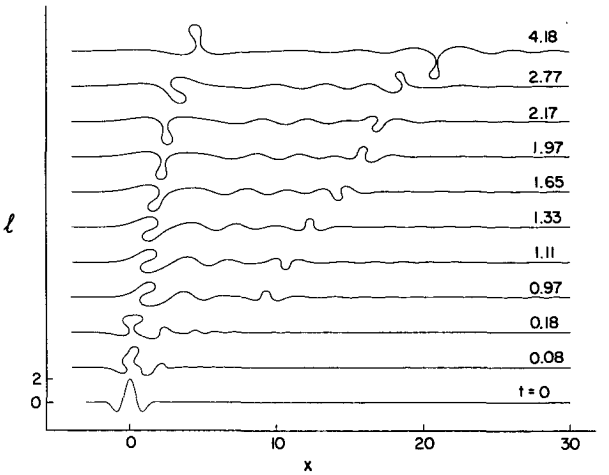

FIG. 9. Numerical solution, Run 9; $a_0 = 2$, $k_0 = 3$, $w = 1$.

velop, one near the origin and the other farther downstream. Both regions experience amplitude growth and both evolve to the point where a single, large lobe is left. The eastern lobe begins to pinch off first, as seen at $t = 4.18$.

Run 6 ($A_0 = 1$, $k_0 = 2$) is the only case exhibiting eddy detachment with an initial condition lying in region I for Fig. 3. Figure 10 shows the maximum values of $|l|$ and $|\partial l/\partial x|$ as functions of time. During the initial phase of evolution ($0 < t < 3$) the maximum slope experiences a sharp increase followed by a decay to approximately one-fourth its initial value. The maximum displacement also decays over this time period. However at $t \approx 3.0$ the maximum slope experiences a sudden increase and multivaluedness ($|\partial l/\partial x| = \infty$) occurs at $t \approx 4.0$. Shortly after l becomes multivalued, the maximum displacement begins to increase and eddy detachment eventually occurs. This example nicely illustrates the coincidence of multivaluedness with the onset of finite amplitude instability. Also, since Run 5 ($A_0 = 1.0, k_0 = 1.5$) does not produce a detaching eddy, the critical value of a_0k_0 for eddy detachment lies between 1.5 and 2.0.

One can define an aspect ratio for the pinching off meander by using the distance between the tip and the point of grazing contact as the long dimension. The aspect ratios for the detaching meanders in Runs 6, 7, 8 and 9; 0.49, 0.47, 0.47 and 0.45 respectively, are quite close.

5. Discussion

Many of the salient properties of the path equation

$$\partial l/\partial t - \tfrac{1}{2}\,\partial \kappa/\partial x = 0 \qquad (5.1)$$

can be illustrated by comparison with the well-known kinematic wave equation

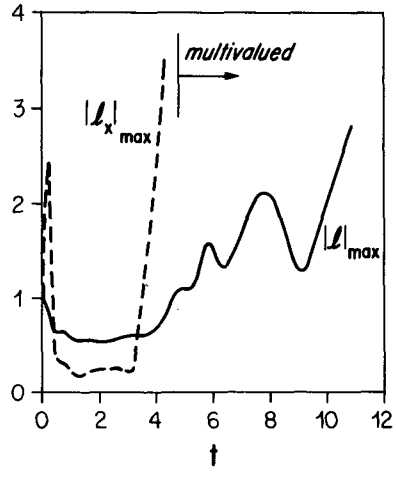

FIG. 10. History of the maximum values of $|l|$ and $|\partial l/\partial x|$ for Run 6.

$$\partial Y/\partial t - U(Y)\partial Y/\partial x = 0 \qquad (5.2)$$

(Whitham 1974). The latter describes the propagation of long waves in a variety of fluid systems. If $dU/dY > 0$, disturbances characterized by large values of Y will "catch up" with those having smaller values of Y due to the mismatch in propagation speed U. This "nonlinear steepening" creates large curvatures and may eventually give rise to irreversible wave breaking phenomena. In some sense the behavior of (5.1) is directly the opposite, as the tendency is for large values of curvature to be dispersed. However, this dispersion results in a more even distribution of curvature $\partial\Theta/\partial s$ over progressively longer segments of arclength, giving rise to more extreme values of Θ, as documented in Section 4. As the front meanders through wider extremes in Θ, different segments come into close proximity and short cross-stream scales arise. In summary both (5.1) and (5.2) have solutions exhibiting singularities associated with short length scales, but the mechanisms by which short lengths are generated are opposite.

It aids the intuition to remember that the only plane curves having uniformly distributed curvature are the line and circle. These curves also happen to be the only steady solutions to (5.1). In the numerical experiments the asymptotic state as $t \to \infty$ for Runs 1–5 is a line. For Runs 6–10 the asymptotic states are akin to combinations of a line and circles (although the detaching blobs are more elliptical than circular). It would be instructive to follow up on this idea further by allowing the blobs to pinch-off and evolve as detached eddies, a calculation which would require extension of the single-contour theory to two contours.

The importance of complicating factors such as the β-effect, short wavelengths, varicose motions, baroclinicity, etc. in most cases of geophysical interest makes it abundantly clear that Eq. (5.1) is *not* a forecast tool. Rather (5.1) determines how flows like the Gulf Stream would evolve in a certain limit and may predict nonlinear tendencies in isolated locations over limited time scales. The fact that (5.1) admits an exact solution whose propagation characteristics reflect measured tendencies for Gulf Stream meanders gives one reason to believe that some of the fundamental physics is captured. However the most important and exciting feature of the calculation is not the reproduction of observed tendencies, but rather the information given regarding the propagation and detachment of more general meanders. In particular, it has been shown that if the characteristic amplitude a_0 and wavenumber k_0 of the isolated initial disturbance (4.3) is such that $(ak)_c < a_0k_0 < 8.30$ (where $ak)_c$ is a value between 1.5 and 2.0), wave breaking occurs followed by amplitude growth of the multivalued meander lobe or lobes. This finite amplitude instability is suggested by the integral constraint (2.7). Eventually one or more roughly elliptical eddies begins to pinch off. For $8.30 < a_0k_0$ (i.e.,

the corresponding periodic solution intersects itself) wave breaking and the pinching effect occur more rapidly with little amplitude growth. The detachment process is initiated when relatively short dispersive waves, emanating from the high-curvature regions near the primary crests and troughs, collide with each other. For $a_0k_0 \approx 8.3$ there undoubtedly exists some intermediate regime for which the secondary waves and finite amplitude instability both play roles.

Some of the numerical integrations presented describe events occurring over such long time periods that other processes would likely intervene in a typical geophysical setting like the Gulf Stream. I particularly refer to the oscillation of the main meander lobes that occurs between $t = 1.79$ and $t = 6.45$ in Fig. 7 and between $t = 2.17$ and $t = 4.18$ in Fig. 9. These times reflect dimensional time scales of several months to a year, and one must worry about the intervention of the β-effect, whose associated time scale $(1/\beta L_d)$ is on the order of several weeks. In numerical studies carried out by Ikeda (1981) and Ikeda and Apel (1981) (summarized in PS) the β-effect is observed to cause a westward movement of the extremities of the meander lobes which enhances detachment. In the flows depicted in Figs. 7 and 9 it is possible that the β-effect could lead to detachment of the oscillating, thin-neck lobes at a much earlier time. Of course, the β-effect also has a stabilizing influence which could suppress the finite amplitude instability. In any case, it would be interesting to investigate the role of the β-effect by performing a calculation similar to that presented herein. Using the formalism of Robinson et al. (1975) it should be possible to derive a long-wave equation governing the motion of a potential vorticity front in a field with nonzero β. Exact solutions and integral constraints analogous to the ones found here could be searched for and, if found, could be used to forecast more general behavior.

Now that the existence of an exact solution at long wavelengths has been established, one can attempt to extend this solution to moderate and small wavelengths using the general equations of contour dynamics (see PS). Should such a solution be found, its stability characteristics might provide criteria for eddy detachment in terms of the wavelength and amplitude of initial disturbances. The ultimate goal is to apply the criteria to intermediate, finite amplitude states observed in other numerical studies of barotropic instability with $\beta = 0$ (e.g., Ikeda 1981; Ikeda and Apel 1981; Flierl et al. 1987), most of which describe evolution in moderate wavelength regimes.

Acknowledgments. This work was supported by the Office of Naval Research under Contract N00014-81-C-0062 and the National Science Foundation (Grant OCE87-00601). Numerical calculations were performed using the Naval Research Laboratory Central Computer Facility. The author would like to thank Drs. B. Cushman-Roisin and W. Young for helpful suggestions concerning the analysis, Dr. D. Haidvogel for suggesting the numerical scheme, and Ms. Barbara Gaffron for help in preparing the manuscript.

APPENDIX A

Derivation of (1.2)

Consider an intrinsic (s^*, η^*) coordinate system in which constant s^* curves are straight lines normal to the front and constant η^* curves are orthogonal to the constant s^* curves (Fig. 11), the asterisk denoting dimensional quantities. The coordinate system is fixed and is determined by the configuration of the front at $t^* = t_0^*$. The position of the front is $\eta^* = \eta_f^*(s^*, t^*)$ and, by definition, the position at $t^* = t_0^*$ is $\eta^* = \eta_f^*(0, t_0^*)$. At subsequent times, the frontal position is

$$\eta_f^*(s^*, t^*) = \eta_f^*(0, t_0^*) + (t^* - t_0^*)\partial\eta_f^*/\partial t_0^* + (t^* - t_0^*)(s^* - s_0^*)\partial^2\eta_f/\partial s_0^*\partial t_0^* + O(t^* - t_2^*)^2. \tag{A1}$$

The dimensional quasi-geostrophic potential vorticity equation (Pedlosky 1979, p. 91) can be written

$$\partial(\zeta^* - fh^*/H)/\partial t^* + \nabla\cdot[\hat{u}^*(\zeta^* - fh^*/H)] = 0 \tag{A2}$$

where f is the Coriolis parameter, H is the mean upper-layer thickness, and h^* ($\ll H$) is the departure of the actual upper-layer thickness from H. Also the quasi-geostrophic velocity $\hat{u}^*$ has s^*- and η^*-components u^* and v^* and

$$v^* = (1 - \kappa^*\eta^*)gf^{-1}\partial h^*/\partial s^*, \qquad u^* = -gf^{-1}\partial h^*/\partial\eta^* \tag{A3a,b}$$

where $\kappa^*(s)$ is the curvature of the front. Finally, ζ^* is the vertical component of vorticity, given in intrinsic coordinates by

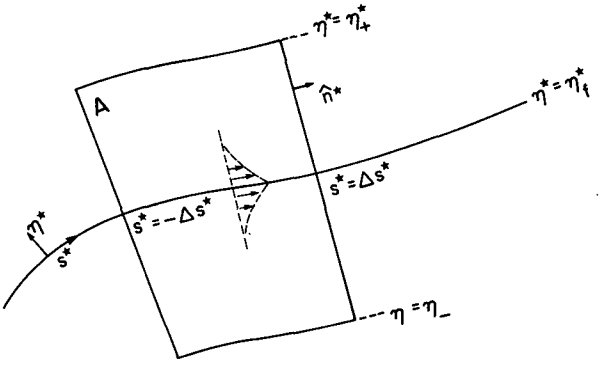

FIG. 11. Integration region defined by fixed intrinsic coordinate system.

$$\zeta^* = (1 - \kappa^*\eta^*)^{-1}\partial v^*/\partial s^* - \partial u^*/\partial \eta^* + \kappa^*(1 - \kappa^*\eta^*)^{-1}u^* \quad \text{(A4)}$$

(Goldstein 1938, p. 119).

If (A2) is integrated over an area A bounded by $\eta^* = \eta_-^*$, $\eta^* = \eta_+^*$ and $s^* = \pm\Delta s^*$, as shown in Fig. 11, the result is

$$\partial/\partial t^* \int_{\eta_-^*}^{\eta_+^*} \int_{-\Delta s^*}^{\Delta s^*} (\zeta^* - fh^*/H)dA + \int_{\eta_-^*}^{\eta_+^*} [(\zeta^* - fh^*/H)(u^* \cdot n^*)]_{s^*=\Delta s^*} d\eta^* - \int_{\eta_-^*}^{\eta_+^*} [(\zeta^* - fh^*/H)(\hat{u}^* \cdot \mathbf{n}^*)]_{s^*=-\Delta s^*} d\eta^* = 0 \quad \text{(A5)}$$

where $\mathbf{n}^*$ is a unit vector pointing outward. The values of $\eta_f^* - \eta_-^*$ and $\eta_+^* - \eta_f^*$ are taken $\gg L_d$, allowing the fluxes of potential vorticity across the boundaries $\eta^* = \eta_-^*$ and $\eta^* = \eta_+^*$ to be neglected.

Now consider the limit of small curvature by requiring that the scale $L_d = (gH)^{1/2}/f$ of variation in the η-direction be small compared to the typical value R of $1/\kappa^*$, so that $\epsilon = L_d/R \ll 1$. The velocity and vorticity can then be approximated as follows:

$$v^* = gf^{-1}[L_d^{-1}\epsilon\partial h^*/\partial(s^*/R) + O(\epsilon^2)] \quad \text{(A6a)}$$

$$u^* = -gf^{-1}L_d^{-1}\partial h^*/\partial(\eta^*/L_d) \quad \text{(A6b)}$$

$$\zeta^* = L_d^{-1}[-\partial u^*/\partial(\eta^*/L_d) + \epsilon(R\kappa^*)u^* + O(\epsilon^2)]. \quad \text{(A7)}$$

Substituting these into (A5), eliminating those terms whose contributions are zero, and retaining only the lowest order terms within each integral leads to

$$\partial/\partial t^* \int_{\eta_-^*}^{\eta_+^*} \int_{-\Delta s^*}^{\Delta s^*} (\kappa^* u^* - fh^*/H)dA + \int_{\eta_-^*}^{\eta_+^*} [\kappa^* u^{*2}]_{s^*=\Delta s^*} - \int_{\eta_-^*}^{\eta_+^*} [\kappa^* u^{*2}]_{s^*=-\Delta s^*} = 0. \quad \text{(A8)}$$

Up to this point the analysis is more or less the same as in Robinson et al. (1975). I now depart from that analysis by formulating the structure of u^* and h^* for the piecewise continuous potential vorticity distribution. To lowest order in ϵ the potential vorticity is described by

$$-\partial u^*/\partial \eta^* - fh^*/H = \begin{cases} -fh_+^*/H, & \eta^* > \eta_f^* \\ -fh_-^*/H, & \eta^* < \eta_f^* \end{cases} \quad \text{(A9)}$$

where h_+^* and h_-^* are the values of h^* as $(\eta^* - \eta_f^*) \to \pm\infty$. Eliminating u^* between (A6b) and (A9) gives

$$\partial^2 h^*/\partial \eta^{*2} - L_d^{-2}h^* = -L_d^{-2}\begin{cases} h_+^*, & \eta^* > \eta_f^* \\ h_-^*, & \eta^* < \eta_f^* \end{cases} \quad \text{(A10)}$$

and this equation leads to the O(0) thickness and velocity profiles

$$h^* = \frac{1}{2}\begin{cases} \Delta h^* \exp[-(\eta^* - \eta_f^*)/L_d] + h_+^*, & \eta^* > \eta_f^* \\ -\Delta h^* \exp[(\eta^* - \eta_f^*)/L_d] + h_-^*, & \eta^* < \eta_f^* \end{cases} \quad \text{(A11)}$$

$$u^* = u_0^* \exp[|\eta^* - \eta_f^*|/L_d] \quad \text{(A12)}$$

where $\Delta h^* = h_+^* - h_-^*$ and $u_0^* = \frac{1}{2}g\Delta h^*/fL_d$.

If (A11) and (A12) are now used to substitute for u^* and h^* in (A8) and η_+^* and η_-^* are taken to $\pm\infty$, the result is

$$-\partial/\partial t^* \int_{-\Delta s^*}^{\Delta s^*} (f/h)[h_+^*(\eta_+^* - \eta_f^*) + h_-^*(\eta_f^* - \eta_-^*)]ds^* + u_0^*[\kappa^*(\Delta s) - \kappa^*(-\Delta s)] \times \int_{-\infty}^{\infty} \exp[2|\eta^* - \eta_f^*|/L_d]d\eta^* = 0.$$

The first integral in the above equation originates from the vortex stretching term $(fH^{-1}\partial h^*/\partial t)$ in the vorticity equation (A2), while the second integral originates from vorticity advection term. Substituting (A1) for η_f^* and letting $t^* \to t_0^*$ and $\Delta s^* \to 0$ leads to

$$(f\Delta h^*/H)\partial \eta_f^*/\partial t - u_0^{*2}L_d\partial \kappa^*/\partial s^* = 0. \quad \text{(A13)}$$

Finally, letting $s^* = sL_d/\epsilon$, $\eta_f^* = l'L_d/\epsilon$, $\kappa^* = \kappa\epsilon/L_d$, $t^* = t\epsilon^{-3}L_d/u_0^*$ and substituting into (A13) gives the desired nondimensional result

$$\partial l'/\partial t - \frac{1}{2}\partial \kappa/\partial s = 0. \quad \text{(A14)}$$

This derivation demonstrates that $\partial l'/\partial t$ is associated with the net vortex stretching in the region, while $\partial \kappa/\partial s$ is associated with the export of vorticity from the region. For an alternative interpretation, consider the equation of mass conservation for the ageostrophic corrections u_a^*, v_a^*, and h_a^* to the velocity and thickness fields (Pedlosky, p. 90). If curvature terms [i.e., terms of $O(\epsilon)$] are neglected, this equation may be written in intrinsic coordinates as

$$\partial h^*/\partial t + \partial(u^*h^*)/\partial s^* + \partial(v^*h^*)/\partial \eta^* + H\partial u_a^*/\partial s + H\partial v_a^*/\partial \eta^* = 0.$$

If this equation is integrated with respect to η^* from $-\infty$ to ∞ and the profiles (A11) and (A12) and the condition $v_a^* = 0$ at $\eta^* = \pm\infty$ are used, the second, third, and fifth terms vanish, leaving

$$(\Delta h^*)\partial \eta_f^*/\partial t + H\int_{-\infty}^{\infty} (\partial u_a^*/\partial s^*)d\eta^* = 0. \quad \text{(A15)}$$

The leading term in (A15) measures volume changes associated with the lateral movement of the deeper, low potential vorticity region relative to the shallower, high potential vorticity region. These changes are balanced in (A15) by a term measuring the divergence of the alongfront ageostrophic velocity. To relate the latter to $\partial\kappa/\partial s$, use the η^*-momentum equation

$$\kappa^* u^{*2} + f u_a^* = -g\partial h_a^*/\partial\eta^* \qquad \text{(A16)}$$

in which $O(\epsilon^2)$ terms, including the time derivative, have been dropped. Integrating (A16) with respect to η^* as before and differentiating the result with respect to s^* leads to

$$\int_{-\infty}^{\infty} (\partial u_a^*/\partial s^*)\, d\eta^* = -u_0^{*2} f^{-1} \partial\kappa^*/\partial s^*.$$

Using this result to substitute for the integral in (A15) leads once again to (A13).

APPENDIX B

Numerical Method

The numerical method for solving Eq. (2.1) is based on a scheme in which spatial derivatives are evaluated using polynomial approximations to the contour. Starting from some location west of the isolated disturbance, the contour is resolved using NP points whose positions at time $t = t_n$ are denoted by $(x_{n,i}, l_{n,i})$ where $i = 1$, NP as shown in Fig. 12. The arclength spacing Δs between points is approximately uniform and the points are numbered so that i increases with increasing arclength beginning with the westernmost point $i = 1$. To calculate the derivative of the curvature of the contour at point $i = j$, one uses new cartesian coordinates x' and y' which are tilted so that x' is tangent to the contour at $i = j$ and points in the direction of increasing s, as in Fig. 12. The front lies at $y' = l'$.

A fifth-order polynomial is then fit through $(x'_{n,j}, l'_{n,j})$ and the nearest four points and the derivative of the curvature is calculated from

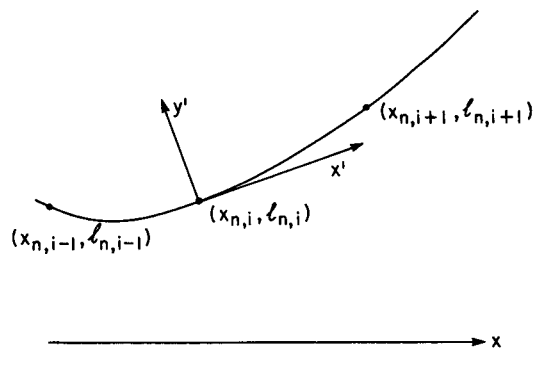

FIG. 12. Sketch showing notation and coordinate system used in numerical algorithm.

$$\frac{\partial\kappa_{n,j}}{\partial s} = \frac{(\partial^3 l'_{n,j}/\partial x'^3)}{[1 + (\partial l'_{n,j}/\partial x')^2]^{3/2}} - \frac{3(\partial l'_{n,j}/\partial x')(\partial^2 l'_{n,j}/\partial x'^2)}{[1 + (\partial l'_{n,j}/\partial x')^2]^{5/2}} \qquad \text{(B1)}$$

using the polynomial to estimate the derivatives of $l_{n,j}$.

Time stepping is implemented using a trapezoidal implicit scheme (Haltiner and Williams 1980). For the equation $u_t = F(u)$ this two-step scheme takes the form

$$u_* = u_{n-1} + 2\Delta t F(u_n)$$

$$u_{n+1} = u_n + \tfrac{1}{2}\Delta t[F(u_n) + F(u_*)]$$

where Δt is the time increment.

For Eq. (2.1) the two steps take the form

$$l'_{*,j} = l'_{n-1,j} + \Delta t\,\partial\kappa_{n,j}/\partial s \qquad \text{(B2)}$$

$$l'_{n+1,j} = l'_{n,j} + \tfrac{1}{4}\Delta t[\partial\kappa_{n,j}/\partial s + \partial\kappa_{*,j}/\partial s] \qquad \text{(B3)}$$

where $\partial\kappa_{n,j}/\partial s$ is calculated from (B1) and $\kappa_{*,j}$ is the curvature based on the provisional values $l'_{*,j}$. For the first ($n = 1$) step $l'_{1,j}$ (and thus $\tau_{1,j}$) can be calculated from

$$l'_{1,j} = l'_{0,j} + \tfrac{1}{2}\Delta t\,\partial\tau_{0,j}/\partial s$$

where $l'_{0,j}$ and $\tau_{0,j}$ are given by the initial conditions.

Since the estimation of $\partial l'/\partial t$ at a given point requires the positions of the two neighboring points on either side, the points $i = 1$, $i = 2$, NP-1, and NP cannot be followed using the main algorithm. For isolated disturbances the value of l and $\partial\kappa/\partial s$ at points $i = 1$ and $i = 2$ can simply be set to zero. At the other end of the domain this specification does not work because waves must be allowed to pass through. After some trial and error the procedure settled upon was to extrapolate l and $\partial\kappa/\partial s$ at points NP and NP-1 from the values at NP-2 and NP-3. Next, the values of l at points NP-4 through NP are reduced by a factor of ½. This condition seemed to allow waves to pass through the boundary without enough reflection to cause a buildup of energy just upstream, as occurred in other schemes.

Although it is difficult to formulate a stability criterion for the fully nonlinear numerical algorithm, one may be guided by the stability criterion for the linear version of Eq. 2.3. According to Haltiner and Williams (1980) this criterion is

$$\Delta t < 2\sqrt{2}\pi^{-3}(\Delta s)^3. \qquad \text{(B4)}$$

In practice, the largest stable value of Δt can be as much as an order of magnitude greater than the value given by (B4). Table 2 lists the maximum stable value of Δt (found by trial and error) for various values of Δs. The actual values of Δs and Δt used for each run are listed in Table 1.

In order to avoid untoward computer expenses, it is important to frequently adjust the space and time steps over the course of each numerical integration. Because of the dispersive character of Eq. (2.1), less and less spatial resolution is required as time progresses and Δs can be increased accordingly. The savings in expense is due to the fact that Δt can be increased in proportion to the third power of Δs (at least). In Run 7, for example, the values of Δs and Δt varied from (0.02, 0.000002) at $t = 0$ to (0.05, 0.00008) at the end.

REFERENCES

Andrews, D. G., and M. E. McIntyre, 1978: On wave action and its relatives. *J. Fluid Mech.*, **89,** 647–664.

Flierl, G. R., and A. R. Robinson, 1984: On the time dependent meandering of a thin jet. *J. Phys. Oceanogr.*, **14,** 412–443.

——, P. Malanotte-Rizzoli and N. J. Zabusky, 1987: Nonlinear waves and coherent vortex structures in barotropic β-plane jets. *J. Phys. Oceanogr.*, **17,** 1408–1428.

Fornberg, B., and G. B. Whitham, 1978: A numerical and theoretical study of certain nonlinear wave phenomena. *Proc. Roy. Soc. London,* **289,** 373–404.

Gear, C. W., 1971: *Numerical Initial Value Problems in Ordinary Differential Equations.* Prentice-Hall, 253 pp.

Goldstein, S., 1938: *Modern Developments in Fluid Mechanics. Vol. 1,* Oxford Press, 702 pp.

Hall, M. M., 1985: Horizontal and vertical structure of velocity, potential vorticity and energy in the Gulf Stream. Ph.D. thesis, Woods Hole Oceanographic Institution and Massachusetts Institute of Technology Joint Program in Oceanography, WHOI-85-16, 165 pp.

Haltiner, G. J., and R. T. Williams, 1980: *Numerical Prediction and Dynamic Meteorology.* Wiley, 477 pp.

Ikeda, M., 1981: Meanders and detached eddies of a strong eastward flowing jet using a two-layer quasi-geostrophic model. *J. Phys. Oceanogr.*, **11,** 526–540.

—— and J. R. Apel, 1981: Mesoscale eddies detached from spatially growing meanders in an eastward-flowing oceanic jet using a two-layer quasi-geostrophic model. *J. Phys. Oceanogr.*, **11,** 1638–1661.

Masuda, A., 1982: An interpretation of the bimodal character of the stable Kuroshio path. *Deep-Sea Res.*, **29,** 471–484.

Overman, E. A., and N. J. Zabusky, 1982: Evolution and merger of isolated vortex structures. *Phys. Fluids,* **25,** 1297–1305.

Pedlosky, J., 1979: *Geophysical Fluid Dynamics.* Springer-Verlag, 624 pp.

Pratt, L. J., and M. E. Stern, 1986: Dynamics of potential vorticity fronts and eddy detachment. *J. Phys. Oceangr.*, **16,** 1101–1120.

Pullin, D. J., 1981: The nonlinear behavior of a constant vorticity layer at a wall. *J. Fluid Mech.*, **108,** 401–421.

Robinson, A. R., J. R. Luyten and G. Flierl, 1975: On the theory of thin rotating jets: A quasi-geostrophic time dependent model. *Geophys. Fluid Dyn.*, **6,** 211–244.

——, M. A. Spall and N. Pinardi, 1988: Gulf Stream simulations and the dynamics of ring and meander processes. *J. Phys. Oceanogr.*, **18,** 1811–1853.

Stern, M. E., 1985: Large scale lateral wave breaking and shingle formation. *J. Phys. Oceanogr.*, **15,** 1274–1283.

—— and L. J. Pratt, 1985: Dynamics of vorticity fronts. *J. Fluid Mech.*, **161,** 513–532.

Timoshenko, S. P., and J. M. Gere, 1961: *Theory of Elastic Stability.* McGraw-Hill, 541 pp.

Tracey, K. L., and D. R. Watts, 1986: On Gulf Stream meander characteristics near Cape Hatteras. *J. Geophys. Res.*, **91,** 7587–7602.

Vazquez, J., and R. D. Watts, 1985: Observations on the propagation, growth, and predictability of Gulf Stream meanders. *J. Geophys. Res.*, **90,** 7143–7151.

Vliegenthart, A. C., 1971: On finite-difference methods for the Korteweg-de Vries equation. *J. Eng. Math.*, **5,** 137–155.

Warren, B. A., 1963: Topographic influences on the path of the Gulf Stream. *Tellus,* **15,** 167–183.

Weatherly, G. L., E. A. Kelley, M. Lopez and R. Harkema, 1984: The Gulf Stream system's frontal position and near bottom flow at the Hebble Site (40°N, 62°W) from January 1982 to September 1982. Florida State University Tech. Rep. 84-01.

Whitham, G. B., 1974: *Linear and Nonlinear Waves.* Wiley and Sons, 636 pp.

Zabusky, N. J., M. Hughes and K. V. Roberts, 1979: Contour dynamics for the Euler equations in two dimensions. *J. Comput. Physics,* **30,** 96–106.